

# Distortions of the posterior surface in optical coherence tomography images of the isolated crystalline lens: effect of the lens index gradient

David Borja,<sup>1,2</sup> Damian Siedlecki,<sup>4,6</sup> Alberto de Castro,<sup>4</sup> Stephen Uhlhorn,<sup>1,2</sup>  
Sergio Ortiz,<sup>4,5</sup> Esdras Arrieta,<sup>1</sup> Jean-Marie Parel,<sup>1,2,3</sup> Susana Marcos,<sup>4</sup> and  
Fabrice Manns<sup>1,2\*</sup>

<sup>1</sup>*Ophthalmic Biophysics Center, Bascom Palmer Eye Institute, University of Miami Miller School of Medicine, 1638 NW 10th Avenue, Miami, Florida 33136, USA*

<sup>2</sup>*Biomedical Optics and Laser Laboratory, Department of Biomedical Engineering, University of Miami College of Engineering, 1251 Memorial Drive, Coral Gables, Florida 33146, USA*

<sup>3</sup>*Vision Cooperative Research Centre, Rupert Myers Building, Sydney, NSW 2052, Australia*

<sup>4</sup>*Instituto de Óptica "Daza de Valdés", Consejo Superior de Investigaciones Científicas, C/Serrano 121, 28006 Madrid, Spain.*

<sup>5</sup>*Laboratorio de Ensayos, Centro de Investigación y Desarrollo de la Armada (CIDA), C/Arturo Soria 289, 28033 Madrid, Spain*

<sup>6</sup>*Institute of Physics, Wrocław University of Technology, Wybrzeże Wyspińskiego 27, 50370 Wrocław, Poland*

\*[fmanns@miami.edu](mailto:fmanns@miami.edu)

**Abstract:** We quantify the posterior surface distortions in optical coherence tomography (OCT) images of isolated crystalline lenses. The posterior radius of curvature and asphericity obtained from OCT images acquired with the beam incident first on the anterior, and then the posterior, surface were compared. The results were compared with predictions of a ray-tracing model which includes the index gradient. The results show that the error in the radius of curvature is within the measurement reproducibility and that it can be corrected by assuming a uniform refractive index. However, accurate asphericity values require a correction algorithm that takes into account the gradient.

©2010 Optical Society of America

**OCIS codes:** (170.4500) Optical coherence tomography; (330.4460) Ophthalmic optics and devices; (330.7326) Visual optics, modeling.

---

## References and links

1. B. K. Pierscionek, and D. Y. Chan, "Refractive index gradient of human lenses," *Optom. Vis. Sci.* **66**(12), 822–829 (1989).
2. R. C. Augusteyn, C. E. Jones, and J. M. Pope, "Age-related development of a refractive index plateau in the human lens: evidence for a distinct nucleus," *Clin. Exp. Optom.* **91**(3), 296–301 (2008).
3. C. E. Jones, D. A. Atchison, R. Meder, and J. M. Pope, "Refractive index distribution and optical properties of the isolated human lens measured using magnetic resonance imaging (MRI)," *Vision Res.* **45**(18), 2352–2366 (2005).
4. P. J. Sands, "Third-order aberrations of inhomogeneous lenses," *J. Opt. Soc. Am.* **60**(11), 1436–1443 (1970).
5. G. Smith, P. Bedggood, R. Ashman, M. Daaboul, and A. Metha, "Exploring ocular aberrations with a schematic human eye model," *Optom. Vis. Sci.* **85**(5), 330–340 (2008).
6. M. Dubbelman, and G. L. Van der Heijde, "The shape of the aging human lens: curvature, equivalent refractive index and the lens paradox," *Vision Res.* **41**(14), 1867–1877 (2001).
7. P. Rosales, M. Dubbelman, S. Marcos, and R. van der Heijde, "Crystalline lens radii of curvature from Purkinje and Scheimpflug imaging," *J. Vis.* **6**(10), 5 (2006).
8. P. Rosales, and S. Marcos, "Pentacam Scheimpflug quantitative imaging of the crystalline lens and intraocular lens," *J. Refract. Surg.* **25**(5), 421–428 (2009).
9. Y. Verma, K. D. Rao, M. K. Suresh, H. S. Patel, and P. K. Gupta, "Measurement of gradient refractive index profile of crystalline lens of fish eye in vivo using optical coherence tomography," *Appl. Phys. B* **87**(4), 607–610 (2007).
10. S. R. Uhlhorn, D. Borja, F. Manns, and J.-M. Parel, "Refractive index measurement of the isolated crystalline lens using optical coherence tomography," *Vision Res.* **48**(27), 2732–2738 (2008).

11. I. Grulkowski, M. Gora, M. Szkulmowski, I. Gorczynska, D. Szlag, S. Marcos, A. Kowalczyk, and M. Wojtkowski, "Anterior segment imaging with Spectral OCT system using a high-speed CMOS camera," *Opt. Express* **17**(6), 4842–4858 (2009).
12. M. C. M. Dunne, L. N. Davies, and J. S. Wolffsohn, "Accuracy of cornea and lens biometry using anterior segment optical coherence tomography," *J. Biomed. Opt.* **12**(6), 064023 (2007).
13. V. Westphal, A. M. Rollins, S. Radhakrishnan, and J. A. Izatt, "Correction of geometric and refractive image distortions in optical coherence tomography applying Fermat's principle," *Opt. Express* **10**(9), 397–404 (2002).
14. A. Podoleanu, I. Charalambous, L. Plesea, A. Dogariu, and R. Rosen, "Correction of distortions in optical coherence tomography imaging of the eye," *Phys. Med. Biol.* **49**(7), 1277–1294 (2004).
15. M. Zhao, A. N. Kuo, and J. A. Izatt, "3D refraction correction and extraction of clinical parameters from spectral domain optical coherence tomography of the cornea," *Opt. Express* **18**(9), 8923–8936 (2010).
16. S. Ortiz, D. Siedlecki, I. Grulkowski, L. Remon, D. Pascual, M. Wojtkowski, and S. Marcos, "Optical distortion correction in optical coherence tomography for quantitative ocular anterior segment by three-dimensional imaging," *Opt. Express* **18**(3), 2782–2796 (2010).
17. R. C. Augusteyn, A. M. Rosen, D. Borja, N. M. Ziebarth, and J.-M. Parel, "Biometry of primate lenses during immersion in preservation media," *Mol. Vis.* **12**, 740–747 (2006).
18. R. Urs, A. Ho, F. Manns, and J. M. Parel, "Age-dependent Fourier model of the shape of the isolated ex vivo human crystalline lens," *Vision Res.* **50**(11), 1041–1047 (2010).
19. F. Manns, V. Fernandez, S. Zipper, S. Sandadi, M. Hamaoui, A. Ho, and J. M. Parel, "Radius of curvature and asphericity of the anterior and posterior surface of human cadaver crystalline lenses," *Exp. Eye Res.* **78**(1), 39–51 (2004).
20. A. M. Rosen, D. B. Denham, V. Fernandez, D. Borja, A. Ho, F. Manns, J. M. Parel, and R. C. Augusteyn, "In vitro dimensions and curvatures of human lenses," *Vision Res.* **46**(6-7), 1002–1009 (2006).
21. D. Borja, F. Manns, A. Ho, N. Ziebarth, A. M. Rosen, R. Jain, A. Amelinckx, E. Arrieta, R. C. Augusteyn, and J.-M. Parel, "Optical power of the isolated human crystalline lens," *Invest. Ophthalmol. Vis. Sci.* **49**(6), 2541–2548 (2008).
22. A. V. Goncharov, and C. Dainty, "Wide-field schematic eye models with gradient-index lens," *J. Opt. Soc. Am. A* **24**(8), 2157–2174 (2007).
23. A. de Castro, S. Ortiz, E. Gamba, D. Siedlecki, and S. Marcos, "Three-dimensional reconstruction of the crystalline lens gradient index distribution from OCT imaging," *Opt. Express* **18**(21), 21905–21917 (2010).
24. A. Pérez-Escudero, C. Dorronsoro, and S. Marcos, "Correlation between radius and asphericity in surfaces fitted by conics," *J. Opt. Soc. Am. A* **27**(7), 1541–1548 (2010).
25. A. Sharma, D. V. Kumar, and A. K. Ghatak, "Tracing rays through graded-index media: a new method," *Appl. Opt.* **21**(6), 984–987 (1982).

---

## 1. Introduction

The crystalline lens of the eye is an inhomogeneous optical element with a refractive index gradient along both the optical and equatorial axes [1,2]. Recent studies using MRI imaging suggest that the refractive index progressively increases from approximately 1.37 in the outer peripheral cortex to 1.43 in the central nucleus [3]. The refractive index gradient contributes significantly to both paraxial optical properties and higher-order aberrations of the lens [4,5].

The index gradient contributes to optical distortions in images of the crystalline lens acquired *in vivo* or *in vitro* using Scheimpflug imaging [6–8], or optical coherence tomography (OCT) [9–11]. In images acquired *in vivo*, the shape of the anterior lens surface is distorted due to refraction at the cornea [7,12]. Additionally, in images acquired *in vivo* or *in vitro*, the shapes of the posterior lens surface and internal boundaries are distorted due to refraction at the anterior lens surface and internally through the refractive index gradient.

Several correction algorithms, generally relying on a ray-trace through the ocular surfaces and media, have been developed to correct for refractive distortions of the cornea or lens in Scheimpflug imaging [6], and OCT [13,14]. Three-dimensional correction algorithms have been developed only very recently [15,16]. One of the limitations of these correction algorithms is that they rely on ray traces in homogeneous media. Correction algorithms for the crystalline lens assume that the lens is homogeneous, with a fixed refractive index equal to the equivalent index [6,16]. The equivalent index is the refractive index of a homogeneous lens with the same shape and dioptric power as the crystalline lens. Differences in the ray path between the real crystalline lens with its index gradient and the uniform equivalent lens introduce uncertainties in the shape of the internal boundaries and posterior surface produced by the correction algorithms.

The purpose of the present study is to quantify the measurement error introduced in the posterior lens surface of OCT images of the *in vitro* lens due to refraction at the anterior lens

surface and through the refractive index gradient of the lens. Implications for the correction of OCT images of the crystalline lens are discussed.

## **2. Materials and methods**

### *2.1 General description*

Cross-sectional OCT images of isolated human crystalline lenses were acquired with a custom built time domain OCT system. The lens was first imaged with the OCT scanning beam incident on the anterior lens surface (“anterior up” image). The lens was then flipped over and imaged with the OCT scanning beam incident on the posterior lens surface (“posterior up” image). In the “anterior-up” images the posterior lens is distorted due to refraction at the anterior lens surface and due to the index gradient. The “posterior up” image provides the undistorted shape of the posterior lens surface. The effect of the refractive index gradient on the posterior shape of the lens is quantified by comparing the radius of curvature and asphericity of the posterior lens surface obtained from the “anterior up” and “posterior up” images. The results were also compared with the predictions from an optical model of the lens with refractive index gradient.

### *2.2 Donor tissue preparation*

All human eyes were obtained and used in compliance with the guidelines of the Declaration of Helsinki for research involving the use of human tissue. Experiments were performed on 12 lenses from 12 different donor eyes within 1 to 4 days post-mortem (average:  $57 \pm 25$  hours). The donor age ranged from 6 to 90 years (average  $47 \pm 22$  years). The lenses were isolated from the eye and immediately immersed in a small chamber filled with preservation medium (DMEM/F-12, D8437, Sigma, St. Louis, MO) [17]. The lens rests at the bottom of the chamber on a soft rubber o-ring (Buna-N, Small Parts Inc, Miami, FL) which prevents any contact of the lens surface with the chamber wall [10].

### *2.3 Image acquisition*

A custom-built time-domain OCT system which has been described elsewhere was used to acquire cross-sectional images of the whole crystalline lens [10]. The system has  $8\mu\text{m}$  axial resolution,  $60\mu\text{m}$  lateral resolution, and a 7.5mm axial scan length in tissue. The axial and lateral resolutions are sufficient to obtain precise measurements of surface shape. A telecentric beam delivery system produces a flat scan field with a maximum lateral scan length of 20mm. The beam delivery system is mounted on a 3-axis positioning stage and the sample chamber is mounted on a manual 5-axis positioning stage. The axial and lateral position of the lens is first adjusted using a continuous real-time display of the central A-scan as a guide, until the lens is centered (maximum signal strength and maximum separation between the lens anterior and posterior signal peaks). Tilt and tip are then adjusted using real-time B-scan images for guidance.

Once the lens is centered and aligned, a cross-sectional OCT image is acquired first with the lens resting on its posterior surface and with the anterior surface facing the OCT beam (Anterior-Up OCT). The lens is then carefully flipped with a surgical spoon, re-aligned, and a cross-sectional OCT image is acquired with the lens resting on its anterior surface and with the posterior surface facing the OCT beam (Posterior-Up OCT). Each cross-sectional OCT image consists of 500 A-lines acquired over a 10mm lateral scan length with 5000 points per A-line.

### *2.4 OCT image analysis*

An edge-detection program developed in MATLAB (MathWorks, Natick MA) is used to detect the position of the intensity peaks corresponding to the anterior and posterior surfaces of the lens on each A-line of the uncorrected OCT image. Any residual tilt is then corrected using a procedure that has been described elsewhere [18]. Along each A-line of the processed image, the position of the intensity peaks is determined by the optical path length traveled

between the boundaries of interest by a ray entering the measurement chamber in a direction parallel to the optical axis. With the coordinate system and notation of Fig. 1, the uncorrected positions of the first and second surfaces are therefore calculated using Eq. (1):

$$z_1(x) = \frac{d_1(x)}{n_{DMEM}} \quad z_2(x) = z_1(x) + \frac{d_2(x) - d_1(x)}{\langle n_L(x) \rangle} \quad (1)$$

In Eq. (1),  $n_{DMEM} = 1.345$  at 825nm is the group refractive index of DMEM and  $\langle n_L(x) \rangle$  is the average value of the group refractive index of the lens along the ray path, both measured at the central wavelength of the OCT beam ( $\lambda = 825\text{nm}$ ). The average group refractive index of the lens was measured directly using a method described previously [10]. The lengths  $d_1(x)$  and  $d_2(x)$  correspond to the optical distances and the lengths  $z_1(x)$  and  $z_2(x)$  correspond to the actual distances along the ray. The curve  $z_1(x)$  is the corrected shape of the first lens surface. The curve  $z_2(x)$  is the shape of the second lens surface corrected for the refractive index but not for refraction at the first lens surface or within the lens. In the “anterior-up” images, the first surface is the anterior lens surface. In the “posterior-up” images, the first surface is the posterior lens surface. The cross-sectional profiles,  $z_1(x)$  and  $z_2(x)$ , were fit with conic functions over the central 6mm zone to calculate the radius of curvatures ( $R$ ) and asphericity ( $Q$ ) of both lens surfaces [19,20].

To evaluate the measurement repeatability, one lens (age = 6 years) was imaged three times in the anterior up position. The standard deviation was 0.07mm (+/-3.5% of the mean) for the anterior radius of curvature and 0.48mm (+/-13% of the mean) for the posterior surface. A separate analysis shows that this measurement variability is due almost entirely to variability in the lens position between successive measurements, not to the processing algorithm.

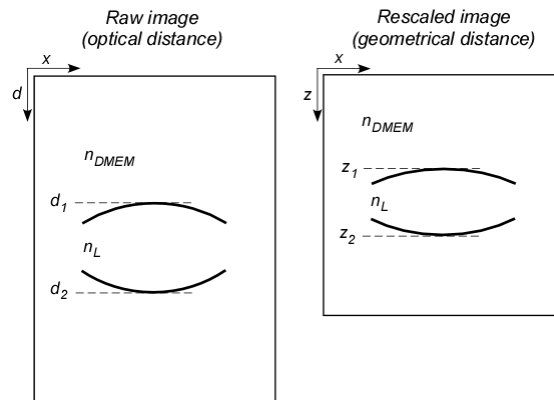


Fig. 1. Optical and geometric location of the lens surfaces in OCT images. Left: Raw image. Right: Image corrected for the refractive index using Eq. (1).

## 2.5. Simulations

### 2.5.1. Effect of the GRIN on distortions

In a first set of simulations, the posterior surface distortions predicted using an exact ray-trace through a homogeneous and GRIN model of the lens were compared with the experimental results. The measured posterior lens surface radius and asphericity obtained from anterior-up images were compared with values obtained from conic fits of the simulated posterior surface. For the homogenous model, simulations were run with two different values of the index: the “average” index and the “best” index. The average refractive index defined in Eq. (1) was obtained by dividing the optical path length in the center of the lens by the actual central lens thickness obtained from shadowphotography images of the same lens [20,21]. The best index

is the homogeneous index that minimizes the RMS error between the measured and simulated posterior lens surface as imaged through the anterior surface. For the GRIN model, we assumed a gradient index distribution based on the three-variable model proposed by Goncharov and Dainty [22]. This model starts with a polynomial expansion of the refractive index function in a meridional plane. Expressions for the coefficients are derived by making assumptions on the shape of the iso-indicial surfaces. The model assumes fixed values for the index of refraction in the core ( $n_c$ ) and the surface ( $n_s$ ) of the lens, and a radius for the posterior isoindicial surface profile ( $r_{pp}$ ) which does not coincide with the radius of the posterior surface.

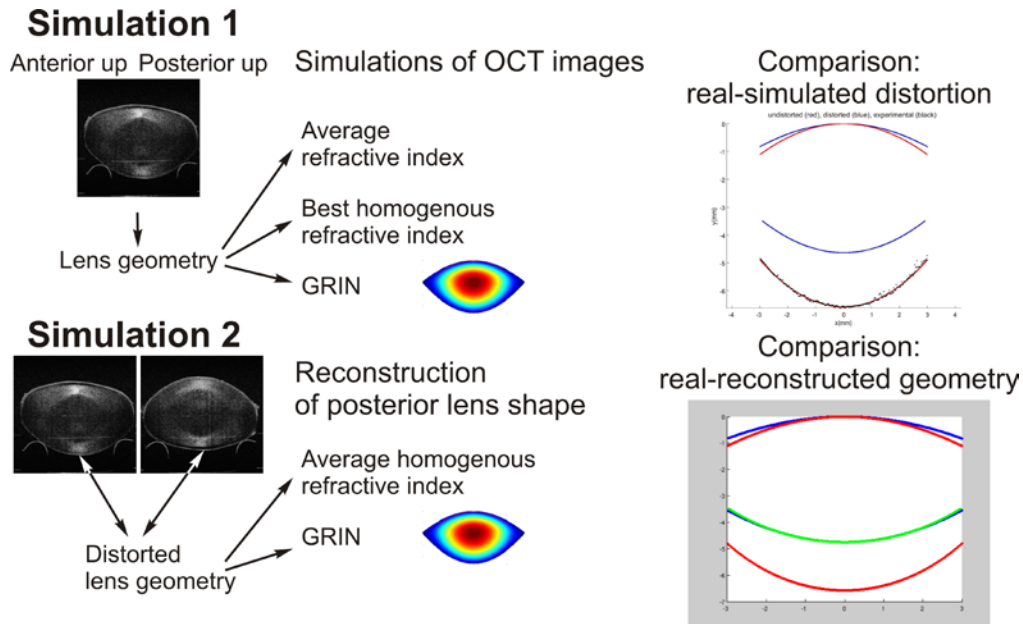


Fig. 2. Schematic diagram of the methods used in the simulations. In Simulation 1 (upper panel) the posterior surface of the lens obtained with OCT is simulated and compared to the measured distorted posterior lens surface, assuming knowledge of the anterior surface (obtained from OCT) and either the measured average refractive index, the best homogeneous index (producing best match with experimental data) and a GRIN distribution in the lens. The figure on the upper right shows the actual lens shape in blue and an example of the simulated distorted shape in red. In simulation 2 (lower panel) distortion correction algorithms are applied to reconstruct the posterior lens shape. The reconstructed shape is compared to the actual geometry obtained by OCT imaging of the flipped-over lens. The algorithm is applied for a homogeneous refractive index and GRIN. The figure in the lower right panel shows the actual lens shape in blue, the distorted lens shape in red, and the reconstructed posterior lens shape in green.

Simulations were performed for a lens from a 6 year old donor using the undistorted lens surface parameters obtained from the anterior and posterior surface up measurements as the nominal values. The measured average index was 1.4191. The gradient index parameters were obtained using a reconstruction method based on optimization of optical path differences, described in detail elsewhere [23], which produced the following values:  $n_c = 1.44319$ ;  $n_s = 1.37351$ ;  $r_{pp} = -3.52546$  mm. Given the potential interactions between radius of curvature and asphericity [24], the differences between the nominal (measured) and simulated surfaces are given in terms of the RMS difference of their elevation. A summary of this simulation is illustrated in the top panel of Fig. 2 (Simulation 1).

### 2.5.2. Effect of the GRIN on distortion correction

A second set of simulations was designed to provide an estimate of the relative contribution of surface refraction and gradient index to the optical distortion Fig. 2 (Simulation 2). In these

simulations, the shape of the undistorted measured posterior lens surface obtained directly from posterior-up images was compared with the shape obtained from anterior-up images after correction using two different methods. In the first method, the distortion is corrected by division by a constant homogenous index of refraction, as in Eq. (1). In the second method, the distortion is corrected using an exact ray-trace assuming both homogeneous and GRIN models, using the same parameters as above. Optical distortion correction in OCT has been described in detail previously for the cornea and lens, and validated using artificial eye models, but the methods were presented only for homogeneous indices of refraction [13,16]. For the posterior surface reconstruction from OCT in the presence of GRIN we have developed here an iterative procedure, which assumes knowledge of the anterior surface shape and the general GRIN distribution, and the posterior surface shape obtained by the simple division by the refractive index method as a starting estimate. The method applies Sharma's algorithm for ray tracing in the GRIN structure [25], and calculates the points that match the optical path measured directly from OCT images, in order to estimate the posterior lens surface in the next iteration. The surface parameters and thickness produce a change in the GRIN distribution in each iteration. The algorithm convergence criterion is established at a difference less than  $0.1 \mu\text{m}$  between the fitting radii of curvature in two successive iterations. The procedure converges rapidly, within in a few iterations. A summary of the reconstruction of the posterior surface shape from the distorted OCT image is presented in Fig. 2, bottom panel.

### 3. Results

#### 3.1 Experimental results

The imaging experiments were successful in all 9 eyes. In 2 eyes, the average group refractive index could not be measured directly. In these two eyes, the index was estimated by using the regression equation as a function of age provided by Uhlhorn et al [10]. Illustrative examples of raw and corrected anterior-up OCT and posterior-up OCT of the same lens are shown in (Fig. 3). Conic section fits provided an accurate description of the central lens profile in all lenses. A Bland-Altman analysis comparing the anterior-up (undistorted) and posterior-up (distorted) measurements of the anterior surface shows that the mean difference ( $\pm 95\%$  confidence interval) between the distorted and undistorted shape is  $0.20 \pm 0.93$  mm for the radius of curvature and  $0.642 \pm 6.153$  for the asphericity (Fig. 4). A similar analysis for the posterior radius produces values of  $0.12 \pm 0.73$  mm for the radius of curvature and  $-0.182 \pm 1.940$  for the asphericity (Fig. 5). Overall the analysis shows that the distorted surface overestimates the true radius of curvature and asphericity. With an error that is within the reproducibility of the measurement.

#### 3.2 OCT Distortion Simulations

We found a substantially good correspondence between the experimental OCT images and the simulated OCT images, assuming a 3-variable Goncharov's GRIN model in the crystalline lens, with the difference between the simulated and measured distorted posterior surfaces being much lower when refraction from the anterior surface and GRIN is considered. Table 1 shows the fitting parameters (radius of curvature and asphericity) of the simulated distortion of the posterior surface when imaged through the lens, and the RMS difference of the nominal and simulated surfaces, with the three different models to distort the image (average refractive index (1.4191); best result for a homogeneous index (1.4168); and assuming refraction through a GRIN index). The best prediction of the distorted surface is obtained when using the GRIN structure. The difference is particularly important in the asphericity of the surface. Figure 6 shows the comparison of the shapes of the simulated distorted surfaces.

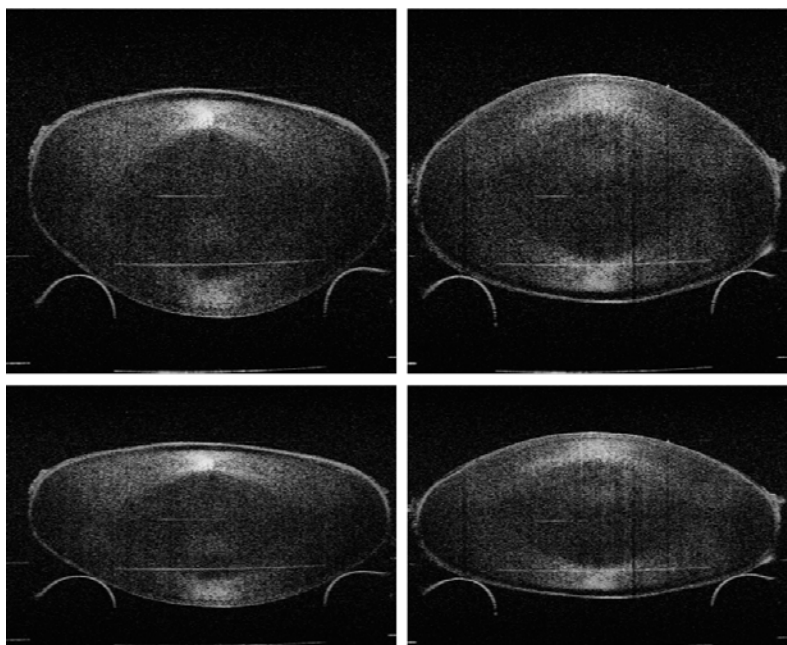


Fig. 3. Raw (top) and rescaled (bottom) OCT images of a 49 year old human crystalline. Left: Anterior-up OCT image; Right: Posterior-up OCT image. Tilt errors are corrected during post-processing before calculating the radius of curvature and asphericity.

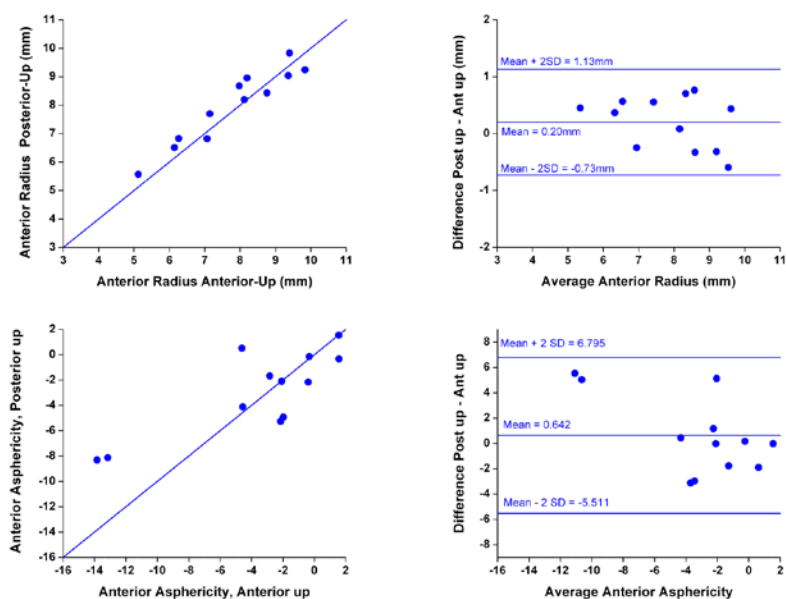


Fig. 4. Bland-Altman analysis of the distorted versus undistorted anterior surface. Top graphs: Radius of curvature; Bottom graphs: Asphericity. The graphs on the left show the distorted parameter (vertical axis) versus the undistorted parameter (horizontal axis). The diagonal is the 1:1 line (perfect correlation). The graphs on the right show for each lens the difference between the distorted and undistorted parameters for each eye versus the average of the two values (mean difference plots). The central horizontal line corresponds to the mean difference. The top and bottom lines correspond to the 95% confidence intervals ( $\pm 2SD$  from the mean).

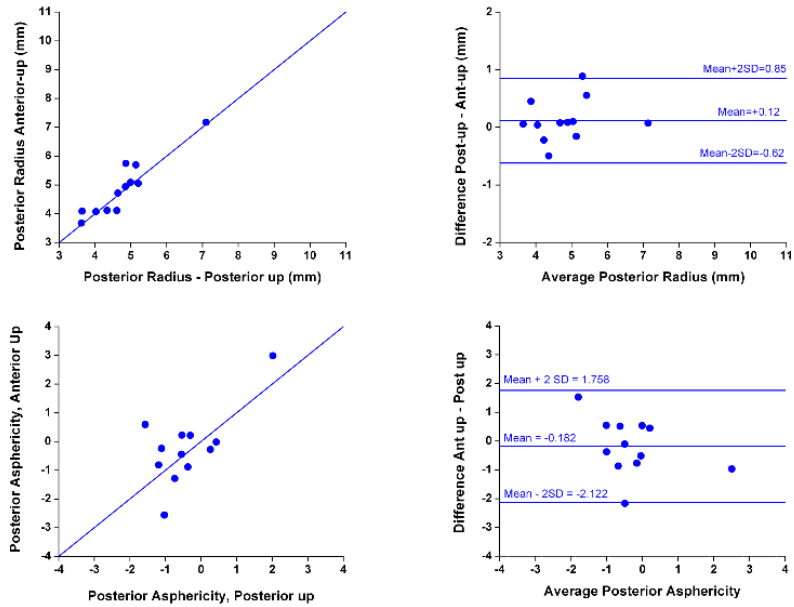


Fig. 5. Bland-Altman analysis of the distorted versus undistorted posterior surface. Top graphs: Radius of curvature; Bottom graphs: Asphericity. The graphs on the left show the distorted parameter (vertical axis) versus the undistorted parameter (horizontal axis). The diagonal is the 1:1 line (perfect correlation). The graphs on the right show for each lens the difference between the distorted and undistorted parameters for each eye versus the average of the two values (mean difference plots). The central horizontal line corresponds to the mean difference. The top and bottom lines correspond to the 95% confidence intervals ( $\pm 2SD$  from the mean).

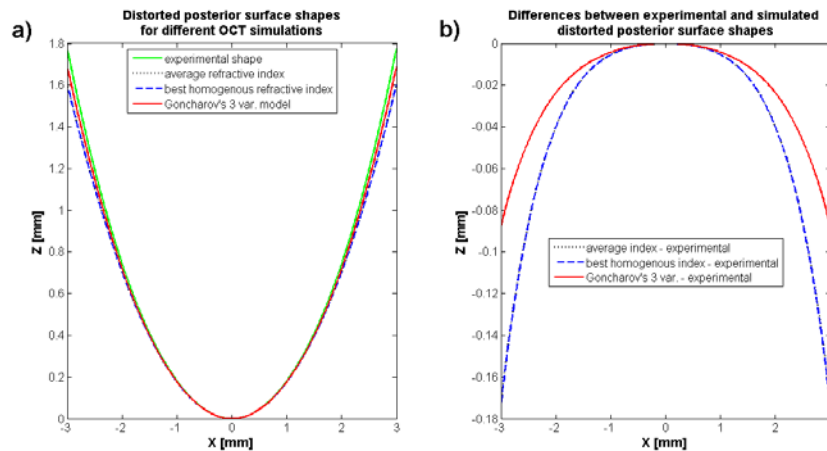


Fig. 6. Simulation results for a lens from a 6 year-old donor. a. Comparison of the actual measured distorted posterior lens contour (experimental shape, in green) with the posterior contour simulated using the three different refractive index models. b. Difference between experimental and simulated distorted posterior surfaces. Average and best homogenous refractive index are hardly distinguishable. The best agreement with the experimental shape is found for the GRIN model.

**Table 1. Measured and simulated distorted posterior surface parameters**

	Measured	Average homogeneous index	Best homogeneous index	Gradient index distribution
Posterior lens radius (mm)	2.792	2.858	2.858	2.852
Posterior lens asphericity	0.289	0.063	0.060	0.219
RMS surface difference (measured-simulated) (mm)	n.a.	0.0257	0.0236	0.0058

**Table 2. Nominal and reconstructed posterior surface parameters. Assuming a refractive index of 1.373 for the lens surface and 1.336 for aqueous, the posterior surface powers are 10.1D (nominal), 9.0D (average index), 10.1D (homogeneous index), 10.3D (GRIN)**

	Nominal	Division by average index	Optical distortion correction homogeneous index	Optical distortion correction GRIN
Posterior lens radius (mm)	3.662	4.120	3.672	3.586
Posterior lens asphericity	-0.135	0.652	0.362	0.034
RMS surface difference (measured-simulated) (mm)	-	0.0224	0.0178	0.0063

### 3.3 OCT Distortion Correction Analysis

In the previous simulations, we estimated how the posterior lens would appear through the lens in an OCT image, and demonstrated that the best prediction of the distorted surface (in comparison with the real distorted surface) is obtained when a GRIN structure is assumed. Different optical distortion correction methods for retrieval of the posterior lens surface through the anterior lens in OCT were investigated as well and retrieved surface parameters were compared to their nominal values. The different OCT processing methods include: (1) simple division of OCT optical paths by an homogeneous index of refraction; (2) refraction by anterior lens surface, assuming a homogeneous index of refraction; and (3) refraction by anterior lens surface, assuming a GRIN index distribution. The corrective iterative method using GRIN provided the most accurate results (Table 2).

The simple division by the value of the average refractive index produced a discrepancy of 0.46mm (12.5%) in the radius of curvature and 0.79 in the asphericity. The incorporation of optical distortion correction methods (refraction by the anterior surface) assuming a homogeneous lens with the average refractive index produced a discrepancy of 0.010mm (0.27%) in the radius of curvature and 0.49 in the asphericity. The correction of refraction from the anterior lens surface assuming a GRIN distribution produced the smallest overall discrepancy: 0.08 mm (2.1%), in the radius of curvature, 0.17 in the asphericity and 0.0063 mm in the RMS surface difference.

## 4. Discussion

Our experimental results show that the distortion due to refraction at the anterior surface and within the gradient produces an error in the posterior radius of curvature that is within the experimental variability of the system. This finding suggests that accurate values of the *in vitro* posterior radius can be obtained by simply rescaling the distances using Eq. (1) with the appropriate value of the index. Experimentally, the average error in the posterior radius of curvature was found to 0.12mm with a 95% confidence interval of 0.73mm, which is very close to the error found with the simulations. The results of the simulations (Table 1 and Table 2) show that most of the error can be corrected by using a ray-tracing procedure assuming a uniform refractive index equal to the average group refractive index of the lens. Interestingly, the optimal refractive index for the correction is closer to the average index than

the equivalent index. The majority of previous studies have used the equivalent index for correction.

The effect of the distortions on asphericity was more variable. For the posterior surface, the distortion produces a mean difference of  $-0.182$ , with a 95% confidence interval of  $\pm 1.9$ . The experimental results suggest that reliable measurements of asphericity of the distorted surface cannot be obtained with the simple correction of Eq. (1). The result of the simulations (Table 2) suggest that a correction algorithm taking into account the GRIN is required to produce accurate values of the asphericity.

Overall, the simulations show that the GRIN makes a significant contribution to the distortion of the posterior surface, particularly in its estimated asphericity. When the GRIN is considered, the simulated posterior surface radius and asphericity are in very good agreement with the measurements obtained through the anterior surface (Table 1). Also, the best reconstruction of the posterior lens surface from OCT images in comparison to the nominal surface (obtained by direct imaging of the posterior surface in “posterior up” position) is obtained when the optical distortion correction algorithm considers the GRIN (Table 2). Interestingly, the results of Table 2 suggest that correction of the optical refraction by the anterior surface using a GRIN model produces a relatively small improvement for the radius of curvature over a model that assumes a homogeneous index of refraction. The presence of GRIN has a larger impact in the reconstruction of the peripheral areas of the lens, as the largest improvements occur for the asphericity estimates.

The results have important implications in the OCT imaging of the crystalline lens, as the presence of GRIN will alter the estimated shape of the posterior lens surface. Our results suggest that for *in vitro* OCT measurements, where the posterior lens surface can be visualized directly by flipping the lens (and therefore having a measurement of the undistorted and distorted posterior lens surface), the calculated distortion could be used to reconstruct the GRIN of the lens. We have recently demonstrated a method that uses the optical path difference distortions in OCT to reconstruct *in vitro* the 3-D GRIN distribution in the porcine lens [23], and the 2-D GRIN distribution in the human lens of various ages.

In the current study, we used the Goncharov 3-variable model to describe the GRIN. While it is not the only possible GRIN lens model (we have obtained similar results with a different 3-variable model), choosing an adequate GRIN model that is representative of the actual lens gradient is critical. Simpler models, such as Goncharov’s 2-variable models, failed to reproduce the distortion of the posterior surface.

In summary, we show that the GRIN produces significant distortions of the posterior shape of the lens, particularly in the lens periphery. However, when imaging *in vitro* lenses, accurate values of the central radius of curvature can be obtained using a simple correction that does not take into account refraction. The distortions can be predicted and corrected using a ray-tracing algorithm that incorporates an adequate model of the GRIN of the lens. Correction algorithms that assume a homogeneous index provide accurate values of the radius of curvature, but not of the asphericity. It is important to remember that these findings are applicable to *in vitro* studies. When imaging the lens *in vivo*, refraction by the cornea may induce significant additional distortions in both the radius and the asphericity.

### Acknowledgments

The authors are grateful to Bianca Maceo and Raksha Urs for assistance with data processing. The study was supported in part by National Eye Institute Grants 2R01EY14225, 5F31EY15395 (NRSA Individual Predoctoral Fellowship, Borja), P30EY14801 (Center Grant); the Florida Lions Eye Bank; the Henri and Flore Lesieur Foundation (JMP); an unrestricted grant from Research to Prevent Blindness and the Vision Cooperative Research Centre, Sydney, New South Wales, Australia, supported by the Australian Federal Government through the Cooperative Research Centres Programme; and grants FIS2008-02065, (Ministerio de Ciencia e Innovación, Spain), EURYI-05-102-ES (EURHORCs-ESF), CSIC I3P Predoctoral and JAE-DOC Postdoctoral Programs.